

---

# RIEMANNIAN LYAPUNOV OPTIMIZER: A UNIFIED FRAMEWORK FOR OPTIMIZATION

---

**Yixuan Wang\*, Omkar Sudhir Patil, Warren E. Dixon**

Department of Mechanical and Aerospace Engineering  
University of Florida

{wang.yixuan, patilomkarsudhir, wdixon}@ufl.edu

## ABSTRACT

We introduce Riemannian Lyapunov Optimizers (RLOs), a family of optimization algorithms that unifies classic optimizers within one geometric framework. Unlike heuristic improvements to existing optimizers, RLOs are systematically derived from a novel control-theoretic framework that reinterprets optimization as an extended state discrete-time controlled dynamical system on a Riemannian parameter manifold. Central to this framework is the identification of a Normally Attracting Invariant Manifold (NAIM), which organizes training dynamics into two distinct stages: rapid alignment of the speed state to a target graph, followed by controlled evolution within it. We formalize this by constructing a strict Lyapunov function that certifies convergence to a target manifold. This perspective yields a constructive “optimizer generator” that not only recovers classic algorithms but enables the principled design of RLOs. We validate our theory via geometric diagnostics and demonstrate that grounding optimizer design in control theory yields state-of-the-art performance in large-scale benchmarks. Overall, RLOs bridge control theory and modern machine learning optimization, providing a unified language and a systematic toolkit for designing stable, effective optimizers.

## 1 Introduction

The evolution of deep learning optimization has produced a vast ecosystem of algorithms designed to navigate complex loss landscapes [1, 2, 3]. This lineage includes Stochastic Gradient Descent (SGD) [4, 5], momentum methods [6, 7], Nesterov’s Accelerated Gradient (NAG) [8], and a diverse array of adaptive methods such as AdaGrad [9], RMSProp [10], Adam [11], AdamW [12], and Adafactor [13]. Recently, specialized techniques like Lion [14], Shampoo [15], and Sophia [16] have pushed the boundaries of efficiency in large scale training by utilizing sign based updates [17, 18] or second order information [19]. While these methods are empirically excellent and form the backbone of modern machine learning, they are largely treated as a collection of distinct heuristics. Theoretical analyses of these optimizers remain fragmented, often focusing on narrow properties or specific algorithmic artifacts [20, 21] while failing to provide a global, principled explanation for their shared success.

Previous attempts to unify accelerated methods often leverage continuous time limits that approximate discrete iterations by second order damped dynamics, providing interpretable surrogate models for rate and stability [22, 23]. Other works have explored unified frameworks through the lens of proximal operators [24] or mirror descent [25], yet these perspectives typically analyze algorithms through fixed time rescalings or simplified state representations, and therefore, do not directly synthesize feedback laws that explicitly regulate the evolution of auxiliary optimizer states. As a result, they do not provide a constructive mechanism level explanation for the observed separation between fast residual alignment and slower descent, especially in discrete time with time varying preconditioning and stochastic gradients. This lack of a cohesive geometric and control theoretic foundation limits our ability to systematically design new optimizers that are both stable and effective across different architectures.

In this paper, we answer the key open question: *Is there a unified geometric principle that governs the stability and efficacy of these diverse optimizers?* We introduce a unified framework that reinterprets optimization as a closed loop

---

\*Corresponding author.

controlled dynamical system on a Riemannian manifold. Our motivation is grounded in the observation of two timescale dynamics where the system state must track a specific relationship between its velocity and the gradient field. We formalize this using the concept of a Normally Attracting Invariant Manifold (NAIM), which serves as the geometric skeleton relating the update speed to the target direction field. Drawing inspiration from the idea of backstepping in nonlinear control theory [26, 27, 28], we construct a strict Lyapunov function that encodes both the objective value and the distance to the NAIM. This approach allows us to derive a controller that actively forces the system to track the manifold, transforming optimizer design from heuristic experimentation into a principled synthesis of Lyapunov based feedback laws. Our contributions lie on:

**(i) Unified Riemannian Geometry:** We demonstrate that diverse optimization components are equivalent to fundamental geometric objects where preconditioning corresponds to selecting a Riemannian metric and momentum represents an extended velocity state in the tangent bundle.

**(ii) The NAIM Mechanism:** We introduce the NAIM as the primary structure organizing training dynamics, proving that optimization consists of a fast process of backstepping the speed state to a target graph followed by a slow drift along that manifold.

**(iii) Strict Lyapunov Design:** We provide a systematic methodology for designing the RLO family of optimizers by synthesizing control laws that satisfy strict Lyapunov requirements using a Riemannian backstepping approach, ensuring robust convergence even under the disturbances typical of stochastic gradients.

This framework provides a blueprint for optimization algorithm design from the perspective of controller design and paves the way for principled innovations. The remainder of the paper is organized as follows: All the notation used in this paper are summarized in Appendix A, Section 2 introduces the Riemannian configuration and builds the optimization as a dynamical system. Section 3 and 4 present our unified framework, and an RLO family based on this framework. Section 5.1 provides empirical validation of the framework. And finally, Section 6 details large scale experimental results.

## 2 Geometric Setup and Problem Formulation

We study the minimization of a differentiable objective function  $f: \mathcal{M} \rightarrow \mathbb{R}$  over a smooth  $n$  dimensional parameter manifold  $\mathcal{M}$  endowed with a Riemannian metric  $g$ . The optimal value of  $f$  is denoted by  $f^*$ , which may be unknown. Discrete time is indexed by  $k \in \mathbb{N}$ .

### 2.1 The Riemannian Configuration

For each  $\theta \in \mathcal{M}$ , let  $T_\theta \mathcal{M}$  denote the tangent space at  $\theta$ . The Riemannian metric assigns an inner product  $g(\cdot, \cdot)$  on  $T_\theta \mathcal{M}$ , and the induced norm is

$$\|\xi\|_{g_\theta} \triangleq \sqrt{g_\theta(\xi, \xi)}, \quad \xi \in T_\theta \mathcal{M}.$$

The Riemannian gradient of  $f$  at  $\theta$ , denoted  $\text{grad } f(\theta) \in T_\theta \mathcal{M}$ , is defined by the identity

$$df(\theta)[\xi] = g_\theta(\text{grad } f(\theta), \xi)$$

for all  $\xi \in T_\theta \mathcal{M}$ , where  $df(\theta)[\xi]$  is the directional derivative of  $f$  at  $\theta$  along  $\xi$ .

To perform iterative optimization, we require a mechanism to map tangent vectors back onto the manifold and to compare vectors across distinct tangent spaces. We employ a retraction  $R$  and a vector transport  $\mathcal{T}$  as our primary computational operators.<sup>2</sup> A retraction is a smooth mapping  $R: T\mathcal{M} \rightarrow \mathcal{M}$  such that for any  $\theta$ , the restriction  $R_\theta: T_\theta \mathcal{M} \rightarrow \mathcal{M}$  satisfies  $R_\theta(0) = \theta$  and its local differential at the origin is the identity map. Furthermore, for any two points  $\theta$  and  $\varphi = R_\theta(\xi)$ , the vector transport  $\mathcal{T}_{\theta \rightarrow \varphi}: T_\theta \mathcal{M} \rightarrow T_\varphi \mathcal{M}$  provides a linear mapping that moves a tangent vector from the source space to the destination space along the retraction curve.

### 2.2 Optimization as an Extended Dynamical System

We conceptualize the optimizer not merely as a rule for updating parameters, but as a controlled dynamical system evolving in an extended state space. We define the system state at time  $k$  as the tuple  $x_k = (\theta_k, v_k, y_k)$ . Here,  $\theta_k \in \mathcal{M}$  represents the current model parameters. The variable  $v_k \in T_{\theta_k} \mathcal{M}$  represents the physical velocity or momentum of the system, residing in the tangent bundle. The variable  $y_k \in \mathcal{Y}$  represents the internal memory state of the optimizer,

<sup>2</sup>When  $\mathcal{M} = \mathbb{R}^n$  with the Euclidean metric, one has  $T_\theta \mathcal{M} = \mathbb{R}^n$ ,  $R_\theta(\xi) = \theta + \xi$  and  $\mathcal{T}_{\theta \rightarrow \varphi}(\xi) = \xi$ . All definitions above reduce to their standard vector space counterparts.

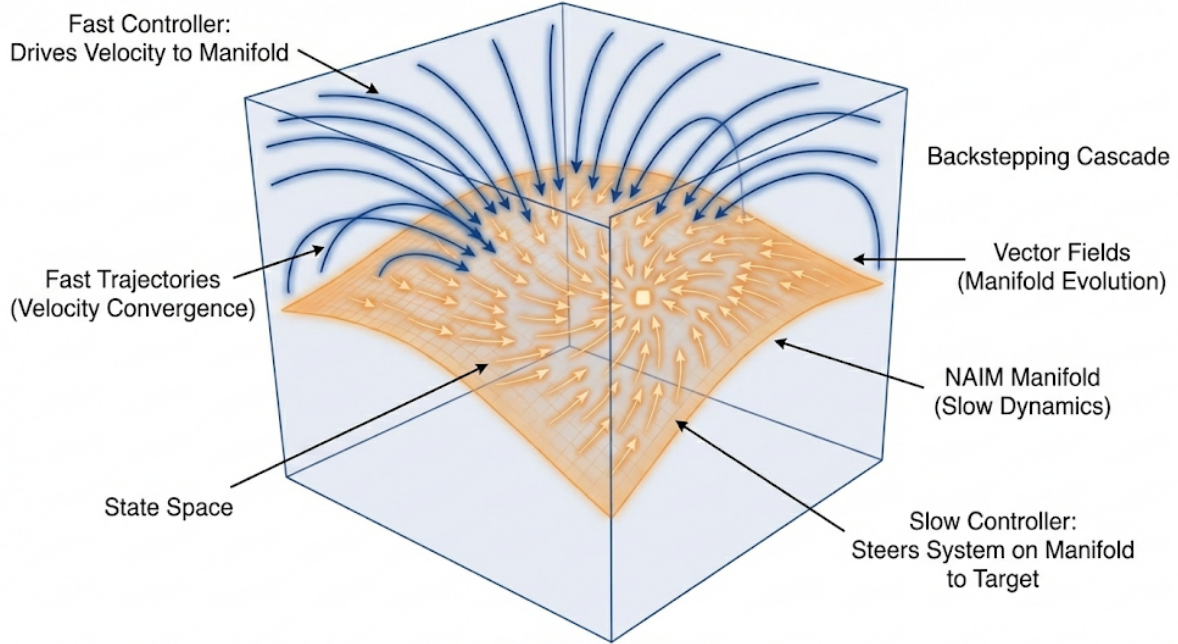


Figure 1: Geometric intuition of the NAIM Lyapunov framework. The orange surface represents the NAIM embedded in the extended state space  $\theta, v$ . Blue streamlines illustrate the fast dynamics: the velocity state  $v$  rapidly contracts onto  $\Lambda$  at a rate governed by the lifting parameter  $\eta$ , regardless of initial conditions. Orange arrows show the slow dynamics: once the trajectory reaches  $\Lambda$ , the system evolves along the direction field  $\Phi$  toward the target optimum at the center.

such as the accumulated first or second moments of the gradients, where  $\mathcal{Y}$  is a vector space appropriate for the selected statistics.

The evolution of this system is governed by an internal state transition map  $\Psi$  and a direction field generator  $\Phi$ . The transition map  $\Psi : \mathcal{Y} \times T\mathcal{M} \rightarrow \mathcal{Y}$  updates the memory state based on the current stochastic gradient. The direction field generator  $\Phi : \mathcal{Y} \times T\mathcal{M} \rightarrow T\mathcal{M}$  constructs a target update direction  $d_k = \Phi(y_k, g_k)$  in the tangent space  $T_{\theta_k} \mathcal{M}$ . This map  $\Phi$  encapsulates the structural logic of the optimizer, including operations such as normalization, clipping, or sign-based transformations. Consequently, a specific optimization algorithm is fully characterized by the tuple  $(\mathcal{M}, g, \Phi, \Psi)$  alongside a sequence of step sizes  $h_k$  and lifting parameters  $\eta_k$ . We rigorously demonstrate in Appendix B that adaptive preconditioning methods in Euclidean space are mathematically equivalent to the selection of a specific time-varying Riemannian metric  $g$ , thereby bringing adaptive optimizers within this geometric framework.

### 3 The NAIM-Lyapunov Framework

Building upon the geometric formulation of the optimizer as an extended dynamical system, we adopt a constructive control perspective. We begin with a generic open-loop mechanical system on the manifold and ask: *What control law is required to force the system to track the NAIM while minimizing the objective function?* We show that the RLO algorithm is not an ad hoc design, but rather a discrete time realization of a Riemannian backstepping controller synthesized within the proposed framework under a strict Lyapunov requirement. Fig 1 illustrates the geometric intuition underlying the framework.

#### 3.1 Open-Loop Dynamics and the Geometric Objective

We model the optimization process as a mechanical system on the tangent bundle  $T\mathcal{M}$ . The open-loop dynamics in continuous time are governed by the covariant equations:

$$\dot{\theta} = v, \quad \nabla_{\dot{\theta}} v = u,$$

where  $\theta \in \mathcal{M}$  is the position,  $v \in T_\theta \mathcal{M}$  is the velocity,  $\nabla$  is the Levi-Civita connection associated with metric  $g$ , and  $u \in T_\theta \mathcal{M}$  is the control input (acceleration) we must design. Our geometric objective is twofold. First, we require the

system to minimize the loss  $f(\theta)$ . Second, we require the physical velocity  $v$  to adhere to the direction field generator introduced in Section 2. This defines the NAIM graph

$$\Lambda = \{(\theta, v) \in T_\theta \mathcal{M} : z \triangleq v - \Phi(y, \text{grad } f) = 0\}.$$

Here,  $z \in T_\theta \mathcal{M}$  is the normal residual. The control problem is to synthesize an input  $u$  that renders  $\Lambda$  attractive and invariant while ensuring  $f(\theta)$  decreases.

### 3.2 Lyapunov-Based Control Synthesis

To synthesize the control law  $u$ , we postulate a strict Lyapunov function candidate  $V$  that encodes a weighted sum of the potential energy (loss) and the kinetic energy of the residual,

$$V(\theta, v, y) = f(\theta) - f^* + \frac{1}{2\lambda} \|z\|_g^2,$$

where  $\lambda > 0$  is a scalar gain parameter (related to the time-scale separation). Taking the time derivative of  $V$  along the trajectories of the open-loop system yields

$$\dot{V} = \langle \text{grad } f, v \rangle_g + \frac{1}{\lambda} \langle z, \nabla_\theta z \rangle_g.$$

Substituting  $v = \Phi + z$  and  $\nabla_\theta z = \nabla_\theta v - \nabla_\theta \Phi = u - \dot{\Phi}$ , we obtain

$$\dot{V} = \underbrace{\langle \text{grad } f, \Phi \rangle_g}_{\text{drift}} + \langle \text{grad } f, z \rangle_g + \frac{1}{\lambda} \langle z, u - \dot{\Phi} \rangle_g.$$

The first term represents the natural descent along the direction field. To guarantee stability ( $\dot{V} < 0$ ), the control input  $u$  must cancel the indefinite terms and enforce decay on  $z$ . A sufficient condition for convergence is to select  $u$  using the principle of geometric backstepping, where the reference velocity is designed as a virtual control input given by the direction field on NAIM. The residual  $z$  then represents the backstepping error, which dynamically couples the position and velocity subsystems through the interaction term  $\langle \text{grad } f, z \rangle_g$ . To render the Lyapunov derivative  $\dot{V}$  strictly negative, the actual control input  $u$  must be synthesized to cancel this destabilizing cross-coupling while simultaneously injecting dissipation into the error dynamics. Accordingly, we choose the control law:

$$u = \underbrace{\nabla_\theta \Phi}_{\text{feedforward}} \underbrace{-\lambda \text{grad } f}_{\text{descent coupling}} \underbrace{-\frac{1}{\tau} z}_{\text{fiber contraction}}.$$

Here,  $\tau > 0$  is the relaxation time constant. The first term  $\nabla_\theta \Phi$  provides the necessary feedforward acceleration to track the evolving target manifold; the second term  $-\lambda \text{grad } f$  is the specific backstepping feedback required to nullify the cross-term  $\langle \text{grad } f, z \rangle_g$ ; and the final term  $-z/\tau$  injects strict damping to contract the residual fiber at a rate determined by the time constant  $\tau$ .

Substituting this control law back into the residual dynamics yields  $\nabla_\theta z = -\frac{1}{\tau} z - \lambda \text{grad } f$ . For small  $\tau$  (fast timescale) and small coupling  $\lambda$ , the dominant behavior is exponential decay:  $\nabla_\theta z \approx -\frac{1}{\tau} z$ .

Substituting the synthesized control  $u$  back into the open-loop plant  $\nabla_\theta v = u$ , we recover the closed-loop dynamics. To implement this, we apply a first-order Euler discretization with time step  $h_k$ . The continuous relaxation  $1/\tau$  maps to the discrete lifting parameter  $\eta_k \in (0, 1]$ , and the term  $\lambda \text{grad } f$  is absorbed into the direction field definition. The continuous fiber contraction  $\nabla_\theta z = -\frac{1}{\tau} z$  discretizes precisely to the update rule

$$z_{k+1} \approx (1 - \eta_k)z_k, \quad \tilde{v}_{k+1} = (1 - \eta_k)v_k + \eta_k \Phi(y_k, g_k).$$

where  $\tilde{v}_{k+1}$  is the lifted speed update computed from  $v_k$  and  $v_{k+1}$  is subsequently updated based on  $\tilde{v}_{k+1}$ . The position update  $\dot{\theta} = v$  discretizes via the retraction:

$$\theta_{k+1} = R_{\theta_k}(-h_k \tilde{v}_{k+1}).$$

Thus, the optimization algorithm designed based on this framework is the numerical approximation of the feedback controller required to stabilize the NAIM.

### 3.3 Lyapunov Stability and Uniform Ultimate Boundedness

In practical settings, the feedforward term  $\nabla_{\dot{\theta}}\Phi$  is often approximated using stochastic gradients, which introduces disturbances in the resulting closed-loop dynamical system. To certify stability under these non-vanishing disturbances, we analyze the discrete Lyapunov difference  $\Delta V_k := V_{k+1} - V_k$ . The goal is to develop a deterministic guarantee that trajectories are confined within a compact set, referred to as a “thick tube,” even under worst-case bounded disturbances.

**Theorem 3.1.** *Consider the RLO system under C.1, C.2 and C.3 regarding smoothness, bounded disturbances, and descent alignment. Consider the discrete RLO dynamics with step size  $h_k$  and lifting parameter  $\eta_k \in (0, 1]$ . Then the following results are obtained.*

**Thick Tube.** *There exists a weighting constant  $\alpha > 0$  such that for sufficiently small  $h_k$ , the discrete Lyapunov function candidate*

$$V_k(\theta_k, z_k) \triangleq f(\theta_k) - f^* + \frac{\alpha}{h_k} \|z_k\|_{g_k}^2$$

*satisfies the difference inequality:*

$$\begin{aligned} V_{k+1} - V_k &\leq -c_1 h_k \|\text{grad } f(\theta_k)\|_g^2 \\ &\quad - c_2 \frac{\eta_k}{h_k} \|z_k\|_g^2 + c_3 \frac{1}{\eta_k h_k} \|\delta_k\|_g^2, \end{aligned}$$

*where  $c_1, c_2, c_3 > 0$  are constants. This implies that the residual  $z_k$  is uniformly bounded by a region proportional to the forcing magnitude  $\|\delta_k\|_g$ , effectively confining the trajectory to a “thick tube” around  $\Lambda$ .*

**Uniformly Ultimate Boundedness.** *If, in addition,  $f$  satisfies the Polyak-Łojasiewicz (PL) condition (C.5) with constant  $\mu_{PL} > 0$ , then the Lyapunov function  $V_k$  converges linearly to a noise floor determined by:*

$$V_{k+1} \leq (1 - \rho)V_k + \frac{c_3}{\eta_k h_k} \|\delta_k\|_g^2,$$

*where  $\rho \in (0, 1)$  is the linear contraction rate. Consequently, the optimization error is ultimately bounded by:*

$$\limsup_{k \rightarrow \infty} (f(\theta_k) - f^*) \leq \limsup_{k \rightarrow \infty} V_k \leq \frac{c_3}{\rho \eta_k h_k} \sup_{t \geq k} \|\delta_t\|_g^2.$$

A complete proof, together with all required assumptions, is provided in Appendix C. This result rigorously validates the “Thick Tube” mechanism: the optimizer establishes a dynamic equilibrium where the Lyapunov contraction balances the disturbances. The tube radius  $\sqrt{\delta_{\max}}$  is explicitly minimized by the smoothness of  $\Phi$ , theoretically justifying why smooth direction fields yield lower steady-state loss than discontinuous ones.

## 4 Unification of Modern Optimizers

The constructive control analysis in Section 3 yields a specific discrete-time feedback controller required to stabilize the NAIM. We formally encapsulate this control logic into the RLO, presented in Algorithm 1. This algorithm serves not merely as a new method, but as a universal computational template determined by four geometric components: the metric  $g$ , the internal state transition  $\Psi$ , the direction field generator  $\Phi$ , and the lifting parameter  $\eta$ .

### 4.1 The RLO Template

Algorithm 1 proceeds in two distinct phases that mirror the two time scales of the dynamics.

The **Geometric Phase** (Lines 3–5) constructs the target manifold  $\Lambda_k$ . Here, the internal state transition  $\Psi$  updates the optimizer’s belief about the landscape geometry (e.g., moment estimation), while the generator  $\Phi$  constructs the target velocity field  $d_k$ . This phase encapsulates *where* the system should ideally move.

The **Dynamic Phase** (Lines 6–8) enforces the convergence update. The physical velocity  $v_k$  relaxes toward  $d_k$  via the fiber contraction rate  $\eta_k$ , and the parameters update along the retracted geodesic. This structure strictly enforces the separation of time scales:  $\Phi$  defines the manifold, while  $\eta$  defines the attraction rate.

### 4.2 Unification via Geometric Components

By instantiating the components  $(\mathcal{M}, g, \Phi, \eta)$ , Algorithm 1 reproduces standard optimizers. We provide a comprehensive mapping in Table 5 (Appendix D), but highlight the structural equivalences here.

---

**Algorithm 1** Riemannian Lyapunov Optimizer (RLO)

---

```
1: Input: Initial  $\theta_0, v_0 = 0$ , state  $y_0$ . Metric  $g$ , Map  $\Phi$ , Transition  $\Psi$ .
2: Hyperparameters: Step sizes  $\{h_k\}$ , lifting rates  $\{\eta_k\}$ .
3: for  $k = 0, 1, \dots, K - 1$  do
4:   // Geometric Phase (Target Construction)
5:   Obtain stochastic gradient  $\hat{g}_k \in T_{\theta_k} \mathcal{M}$ .
6:    $y_{k+1} \leftarrow \Psi(y_k, \hat{g}_k)$                                 {Update internal memory}
7:    $d_k \leftarrow \Phi(y_{k+1}, \hat{g}_k)$                             {Define target vector on  $\Lambda_k$ }
8:   // Dynamic Phase (Manifold Tracking)
9:    $\tilde{v}_{k+1} \leftarrow (1 - \eta_k)v_k + \eta_k d_k$                 {Fiber contraction}
10:   $\theta_{k+1} \leftarrow R_{\theta_k}(-h_k \tilde{v}_{k+1})$                   {Parameter update}
11:   $v_{k+1} \leftarrow \mathcal{T}_{\theta_k \rightarrow \theta_{k+1}}(v_{k+1})$             {Vector transport}
12: end for
```

---

**Adaptive Preconditioning as Metric Selection.** Methods like Adam and RMSProp are rigorously recovered by selecting a time-varying Riemannian metric  $g_k = \text{diag}(\sqrt{s_k})^{-1}$ , where  $s_k$  is the second moment estimate. Under this metric, the standard Adam update is not a heuristic scaling, but the canonical fiber contraction evolving on a geometry that adapts to the local curvature.

**Symbolic Optimizers as Nonlinear Gradient Fields.** Algorithms like Lion utilize the sign operator, breaking the link between update magnitude and gradient norm. In our framework, this corresponds to a nonlinear direction field  $\Phi(y, g) = \text{sign}(y)$ . While this implies  $\Lambda$  is now a nonlinear graph, the Lyapunov stability analysis remains valid provided the forcing term  $\delta_k$  remains bounded.

### 4.3 The RLO Family

To empirically validate the geometric principles of NAIM, we investigate three distinct algorithms derived from the proposed framework; detailed formulations and hyperparameter settings are provided in Appendix D. The primary instantiation, RLO-Lifted, fully realizes the two-time-scale dynamics inherent to the expanded phase space. This algorithm defines the target manifold  $\Lambda$  via a smooth, bounded mapping—specifically a hyperbolic tangent applied to the first moment estimate—and maintains an explicit velocity state  $v_k$  that relaxes toward  $\Lambda$  governed by the lifting parameter  $\eta$ .

To isolate the contribution of the inertial lifting mechanism, we evaluate a degenerate variant denoted simply as RLO. This algorithm represents the greatest contraction where the velocity alignment timescale vanishes ( $\eta \rightarrow 1$ ), forcing the trajectory to evolve directly along the vector field defined by the target graph without the stabilization provided by the fast variable.

Finally, to demonstrate the framework’s capacity to incorporate local geometry into the invariant manifold definition, we introduce RLO- $\Lambda$ . This variant constructs a more sophisticated target graph  $\Phi$  by integrating second-order moment estimates into the mapping; effectively, this variant acts as a geometric preconditioner that reshapes  $\Lambda$  to normalize curvature, resulting in a smoother and more regularized target vector field compared to the standard RLO.

## 5 Geometric Validation of the NAIM Framework

Before demonstrating the performance of RLO on large scale benchmarks, we first validate the theoretical predictions of our framework through carefully designed diagnostic experiments. The goal of this section is twofold: (i) to disentangle the contributions of different algorithmic components through systematic ablation and (ii) to conduct a hyperparameter search on a small dataset to understand the effect of changing learning rate, batch size, and global normalization. All experiments in this section use ResNet-18 [29] on CIFAR-10, with comprehensive hyperparameter details provided in Appendix E together with an  $\eta$  ablation experiment.

### 5.1 Isolating the NAIM Mechanism

**Global Normalization and Contraction Rate.** A natural question arises: does the empirical success of RLO stem from the NAIM geometric structure, or is it merely a consequence of the global normalization that rescales update magnitudes? To answer this question rigorously, we design a factorial ablation based on RLO-Lifted (Algorithm 4) that independently varies two factors: the presence of global normalization and the choice of lifting parameter  $\eta$ .

Table 1: Factorial ablation of RLO-Lifted on CIFAR-10 with ResNet-18 trained for 50 epochs. Each variant is evaluated at its optimal learning rate determined by grid search (see Section 5.2). The Nolifted variants set  $\eta = 1$ , eliminating the explicit velocity state so that  $v_k = d_k$  at every step. GN denotes global normalization, LR denotes the learning rate and Acc denotes accuracy in this and all subsequent tables.

$\eta$	GN	Optimal LR	Best Acc	Final Acc
0.7	✓	$3 \times 10^{-5}$	91.59%	91.21%
0.7	✗	$3 \times 10^{-3}$	89.76%	89.42%
1	✓	$3 \times 10^{-5}$	91.51%	91.13%
1	✗	$3 \times 10^{-3}$	89.02%	88.67%

Table 2: Effect of direction field smoothness on CIFAR-10. The smooth tanh mapping significantly outperforms the discontinuous sign function when global normalization is disabled.

$\Phi$	GN	LR	Best Acc	Final Acc
$\tanh(\gamma c)$	✓	$10^{-4}$	91.69%	91.49%
$\text{sign}(c)$	✓	$10^{-4}$	91.91%	91.91%
$\tanh(\gamma c)$	✗	$3 \times 10^{-3}$	90.74%	90.74%
$\text{sign}(c)$	✗	$3 \times 10^{-3}$	87.15%	74.43%

The global normalization computes scale  $= \sqrt{D}/\|s\|$  where  $D$  is the total parameter count and  $s = \tanh(\gamma c)$  is the pre-normalized direction. This operation projects the update onto a sphere of radius  $\sqrt{D}$ , effectively decoupling the update magnitude from the gradient norm. To isolate its contribution, we compare four variants in a  $2 \times 2$  factorial design: RLO-Lifted ( $\eta = 0.7$ ) versus Nolifted ( $\eta = 1.0$ , where the velocity immediately equals the target direction), crossed with enabled versus disabled the global normalization.

Table 1 presents the main ablation results. Several observations deserve attention. First, the optimal learning rate differs by two orders of magnitude between normalized and unnormalized variants:  $3 \times 10^{-5}$  with global normalization versus  $3 \times 10^{-3}$  without. This confirms that global normalization acts as an implicit learning rate multiplier, amplifying the effective step size by a factor proportional to  $\sqrt{D}/\|s\|$ . For our ResNet-18 architecture with approximately 11 million parameters, this factor is on the order of  $10^2$ .

Second, and more importantly, when each variant is evaluated at its respective optimal learning rate, the performance gap between normalized and unnormalized configurations is modest: 1.83 percentage points for RLO-Lifted and 2.49 points for the Nolifted variant. This outcome demonstrates that global normalization is not the primary source of optimization efficacy. Rather, it serves as a convenient mechanism for automatic learning rate adaptation that can be substituted by manual tuning without fundamental loss of performance.

Third, the comparison between RLO-Lifted and Nolifted ( $\eta = 1$ ) reveals minimal difference in accuracy. At first glance, this might suggest that the lifting mechanism provides no benefit. However, we interpret this finding differently: setting  $\eta = 1$  corresponds to the limiting case of infinitely fast fiber contraction, where the velocity instantaneously aligns with the target direction at every step. The comparable performance indicates that for this benchmark, the NAIM tracking is highly effective regardless of whether alignment occurs gradually ( $\eta < 1$ ) or immediately ( $\eta = 1$ ). Extended analysis of the lifting parameter is provided in Appendix E.1.

**Direction Field Smoothness.** Our theoretical analysis in Section 3 predicts that smoother direction field generators  $\Phi$  should yield more stable optimization by reducing the drift term  $\delta_k$  in the Lyapunov bound. To test this prediction, we modify RLO-Lifted to compare its default smooth hyperbolic tangent  $\Phi = \tanh(\gamma \cdot)$  against the discontinuous sign function  $\Phi = \text{sign}(\cdot)$  used in Lion and the base RLO variant.

Table 2 reveals an interesting asymmetry. Under global normalization, both direction fields achieve comparable accuracy, with the sign function marginally outperforming tanh by 0.22 points. However, when global normalization is removed, the smooth tanh mapping dramatically outperforms the discontinuous sign function: 90.74% versus 87.15% at peak, with an even larger gap at convergence (90.74% versus 74.43%). This 3.59 percentage point difference, and the severe degradation in final accuracy for the sign variant, confirms that smooth direction fields provide substantially more robust optimization when the implicit regularization of global normalization is absent. We provide detailed analysis of this phenomenon in Appendix F.

LR  $\times$  Batch Size Grid Search Results

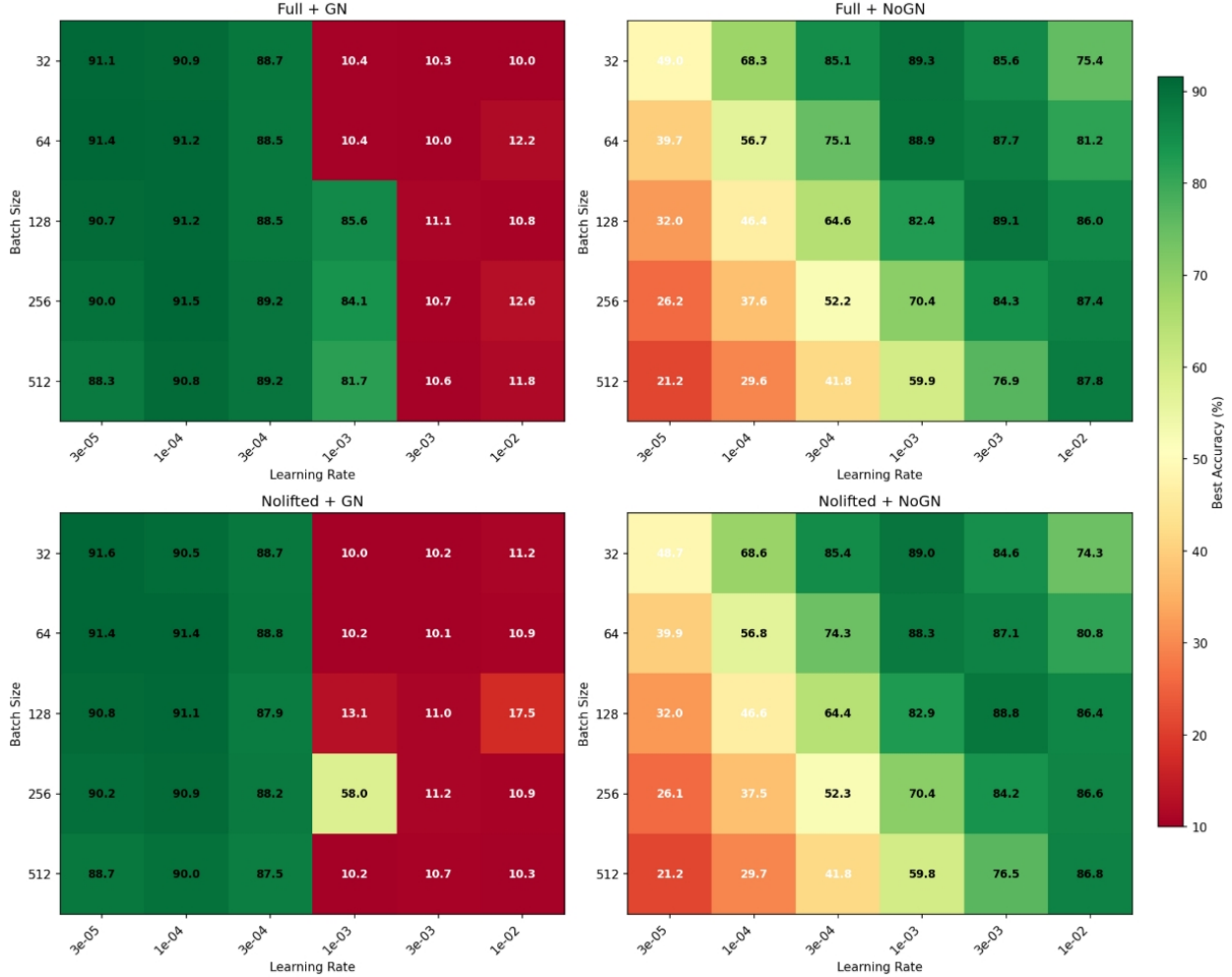


Figure 2: Hyperparameter sensitivity heatmaps for the four factorial variants. Color intensity indicates test accuracy (%). The global normalization enabled variants (left column) achieve peak performance at small learning rates ( $\sim 3 \times 10^{-5}$ ), while the without global normalization variants (right column) require large learning rates ( $\sim 3 \times 10^{-3}$ ). The optimal regions differ by approximately two orders of magnitude in the learning rate axis.

## 5.2 Hyperparameter Sensitivity Analysis

To understand the interaction between global normalization and standard hyperparameters, we conduct a comprehensive grid search over learning rates and batch sizes for each of the four factorial variants.

Figure 2 visualizes the results as heatmaps. The most striking pattern is the systematic shift in optimal learning rate between normalized and unnormalized variants. With global normalization enabled, peak accuracy occurs in the leftmost columns corresponding to learning rates around  $3 \times 10^{-5}$ , and performance collapses entirely for learning rates exceeding  $10^{-3}$ . Without global normalization, this pattern inverts: small learning rates yield accuracy near random chance (around 32%), while competitive performance requires learning rates of  $10^{-3}$  or larger.

Beyond the learning rate shift, we observe that all the variants are not sensitive to the batch size. This interaction may reflect the relationship between gradient noise variance, and the regularizing effect of global normalization.

The heatmaps also reveal sharp stability boundaries for the global normalization enabled variants. At learning rates exceeding  $3 \times 10^{-4}$ , accuracy drops precipitously to random chance levels, indicating that the effective step size has exceeded the basin of attraction. This boundary corresponds to the point where the implicit amplification factor  $\sqrt{D}/\|s\|$

Table 3: ImageNet-1K classification results (Top-1 accuracy %). All models trained for 90 epochs with cosine learning rate schedule. Best results in **bold**, second best underlined.

Optimizer	ResNet-50	ViT-S/16	ViT-B/16
AdamW	73.87	75.18	71.42
LION	73.36	75.14	<u>76.27</u>
RLO	73.45	<u>75.38</u>	76.00
RLO- $\Lambda$	<b>73.98</b>	<b>76.18</b>	<b>76.47</b>
RLO-Lifted	<b>73.98</b>	71.43	76.33

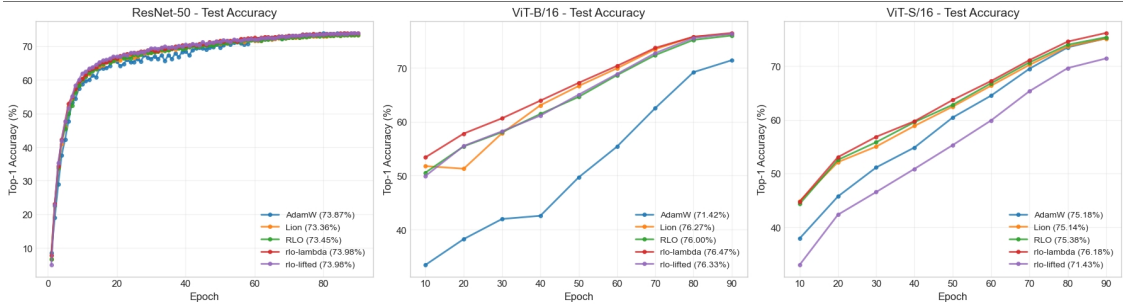


Figure 3: Validation accuracy curves for ImageNet classification using ResNet-50 (left), ViT-B/16 (center), and ViT-S/16 (right). RLO- $\Lambda$  consistently achieves the highest final accuracy across all architectures (73.98%, 76.47%, 76.18% respectively). Notably, sign-based optimizers (Lion, RLO variants) demonstrate substantially faster convergence and higher final accuracy than AdamW on Vision Transformers, suggesting that the NAIM-guided updates are particularly effective for attention-based architectures.

pushes the actual parameter displacement beyond the region where the loss landscape can be locally approximated. In contrast, the without global normalization variants degrade more gracefully at both extremes of the learning rate range, suggesting that explicit control over step size provides more predictable behavior even if it requires more careful tuning. We provide further details in Appendix E and additional ablation analysis in Appendix F.

With this foundation established, Section 6 evaluates RLO on large scale benchmarks where computational constraints preclude exhaustive hyperparameter search.

## 6 Large-Scale Benchmarks

Having validated the geometric mechanisms underlying RLO in Section 5, we now evaluate its performance on large-scale benchmarks that test whether these principles translate to practical gains. We follow the experimental protocol established by [14], comparing RLO variants against AdamW and Lion on ImageNet classification [30] with both convolutional and transformer architectures. Complete hyperparameter configurations and training details are provided in Appendix G.

### 6.1 ImageNet Classification

We evaluate three architectures that span different inductive biases and model scales: ResNet-50 representing convolutional networks, ViT-S/16 [31], and ViT-B/16 [32]. All models are trained from scratch for 90 epochs on ImageNet-1K with a global batch size of 1024, using cosine learning rate decay with linear warmup during the first 5 epochs. Following the protocol in [14], we tune learning rates and weight decay independently for each optimizer to ensure fair comparison. The test accuracy curves for all three models are presented in Fig 3. Table 3 presents the main classification results. Several patterns emerge from this comparison that illuminate both the strengths and the boundaries of our framework.

**Convolutional Networks.** On ResNet-50, all optimizers achieve similar performance within a narrow range of 0.62 percentage points. RLO- $\Lambda$  and RLO-Lifted tie for the best accuracy at 73.98%, marginally outperforming AdamW (73.87%), RLO (73.45%), and Lion (73.36%). This near-parity is consistent with prior findings that convolutional architectures are relatively insensitive to optimizer choice when hyperparameters are well-tuned, likely because the

strong inductive biases of convolution constrain the optimization landscape to be relatively benign regardless of the descent direction.

**Vision Transformers.** The transformer architectures reveal more pronounced differences that highlight the importance of our geometric framework. On ViT-S/16, RLO- $\Lambda$  achieves 76.18%, outperforming AdamW by 1.0 percentage point, Lion by 1.04 points, and the base RLO by 0.8 points. The advantage of RLO- $\Lambda$  is even more pronounced when considering the gap to the worst-performing method: RLO-Lifted achieves only 71.43% on this architecture, a deficit of 4.75 points relative to RLO- $\Lambda$ .

On the larger ViT-B/16, the ranking shifts notably. RLO- $\Lambda$  again achieves the highest accuracy at 76.47%, but now RLO-Lifted recovers to 76.33%, closely followed by Lion at 76.27% and base RLO at 76.00%. Most strikingly, AdamW substantially underperforms at 71.42%, a gap of over 5 percentage points compared to RLO- $\Lambda$ . This dramatic difference aligns with observations in [14] that sign-based optimizers can significantly outperform adaptive methods on vision transformers when training for a fixed number of epochs.

The consistent strong performance of RLO- $\Lambda$  across all three architectures supports the theoretical framework developed in Sections 3 and 4. The adaptive preconditioning in RLO- $\Lambda$ , which constructs the target manifold  $\Lambda$  using second-moment information, appears to provide robust benefits across different model families. The scale-dependent behavior of RLO-Lifted, which performs well on ResNet-50 and ViT-B/16 but poorly on ViT-S/16, suggests that the optimal lifting parameter  $\eta$  may depend on model capacity in ways that warrant further investigation. We conjecture that smaller models require faster adaptation to rapid landscape changes, which the explicit velocity state in RLO-Lifted may impede. Detailed ablation on this hypothesis is provided in Appendix H.

## 7 Conclusion

This paper develops a unified geometric framework for understanding and designing optimization algorithms in machine learning. By interpreting optimization as an extended-state control problem on a Riemannian manifold, we establish a principled foundation that reveals structural connections among seemingly disparate methods and enables systematic construction of new algorithms with provable guarantees.

This NAIM-Lyapunov framework characterizes optimizers through three geometric objects: a Riemannian metric  $\mathcal{M}$ , a direction field generator  $\Phi$ , and a contraction rate  $\eta$ . This abstraction recovers existing methods as special cases: SGD with momentum, Adam, and Lion all emerge from specific instantiations of these components. The framework thus provides a generative grammar for optimization algorithms rather than merely a post-hoc taxonomy. The Lyapunov-based construction methodology transforms optimizer design from heuristic experimentation into strict Lyapunov controller design. Beginning with open-loop gradient dynamics, we construct a Lyapunov function certifying convergence, derive a control law guaranteeing  $\dot{V} < 0$ , and obtain closed-loop dynamics whose discretization yields the update rule. This synthesis ensures that resulting algorithms inherit stability properties from the continuous-time analysis.

Systematic ablation validates that the NAIM geometric structure provides optimization benefits independent of auxiliary mechanisms, while large-scale experiments demonstrate that RLO- $\Lambda$  achieves the best average performance over ImageNet classification benchmarks.

## 8 Acknowledgment

This research is based on work supported in part by AFOSR grant FA9550-19-1-0169, AFRL grant FA8651-21-F-1027, and Office of Naval Research Grant N00014-13-1-0151. Any opinions, findings and conclusions or recommendations expressed in this material are those of the author(s) and do not necessarily reflect the views of the sponsoring agency.

## References

- [1] Nitish Shirish Keskar, Dheevatsa Mudigere, Jorge Nocedal, Mikhail Smelyanskiy, and Ping Tak Peter Tang. On large-batch training for deep learning: Generalization gap and sharp minima. *arXiv preprint arXiv:1609.04836*, 2016.
- [2] Hao Li, Zheng Xu, Gavin Taylor, Christoph Studer, and Tom Goldstein. Visualizing the loss landscape of neural nets. *Advances in neural information processing systems*, 31, 2018.
- [3] Léon Bottou, Frank E Curtis, and Jorge Nocedal. Optimization methods for large-scale machine learning. *SIAM review*, 60(2):223–311, 2018.

- [4] Herbert E. Robbins. A stochastic approximation method. *Annals of Mathematical Statistics*, 22:400–407, 1951.
- [5] Pratik Chaudhari, Anna Choromanska, Stefano Soatto, Yann LeCun, Carlo Baldassi, Christian Borgs, Jennifer Chayes, Levent Sagun, and Riccardo Zecchina. Entropy-sgd: Biassing gradient descent into wide valleys. *Journal of Statistical Mechanics: Theory and Experiment*, 2019(12):124018, 2019.
- [6] B.T. Polyak. Some methods of speeding up the convergence of iteration methods. *USSR Computational Mathematics and Mathematical Physics*, 4(5):1–17, 1964.
- [7] Ilya Sutskever, James Martens, George Dahl, and Geoffrey Hinton. On the importance of initialization and momentum in deep learning. In Sanjoy Dasgupta and David McAllester, editors, *Proceedings of the 30th International Conference on Machine Learning*, volume 28 of *Proceedings of Machine Learning Research*, pages 1139–1147, Atlanta, Georgia, USA, 17–19 Jun 2013. PMLR.
- [8] Aleksandar Botev, Guy Lever, and David Barber. Nesterov’s accelerated gradient and momentum as approximations to regularised update descent. In *2017 International joint conference on neural networks (IJCNN)*, pages 1899–1903. IEEE, 2017.
- [9] John Duchi, Elad Hazan, and Yoram Singer. Adaptive subgradient methods for online learning and stochastic optimization. *Journal of Machine Learning Research*, 12(61):2121–2159, 2011.
- [10] T. Tieleman. Lecture 6.5-rmsprop: Divide the gradient by a running average of its recent magnitude, 2012.
- [11] Diederik P Kingma. Adam: A method for stochastic optimization. *arXiv preprint arXiv:1412.6980*, 2014.
- [12] Ilya Loshchilov and Frank Hutter. Decoupled weight decay regularization. *arXiv preprint arXiv:1711.05101*, 2017.
- [13] Noam Shazeer and Mitchell Stern. Adafactor: Adaptive learning rates with sublinear memory cost. In *International Conference on Machine Learning*, pages 4596–4604. PMLR, 2018.
- [14] Xiangning Chen, Chen Liang, Da Huang, Esteban Real, Kaiyuan Wang, Hieu Pham, Xuanyi Dong, Thang Luong, Cho-Jui Hsieh, Yifeng Lu, et al. Symbolic discovery of optimization algorithms. *Advances in neural information processing systems*, 36:49205–49233, 2023.
- [15] Vineet Gupta, Tomer Koren, and Yoram Singer. Shampoo: Preconditioned stochastic tensor optimization. In *International Conference on Machine Learning*, pages 1842–1850. PMLR, 2018.
- [16] Hong Liu, Zhiyuan Li, David Hall, Percy Liang, and Tengyu Ma. Sophia: A scalable stochastic second-order optimizer for language model pre-training. *arXiv preprint arXiv:2305.14342*, 2023.
- [17] Jeremy Bernstein, Yu-Xiang Wang, Kamyar Azizzadenesheli, and Animashree Anandkumar. signsgd: Compressed optimisation for non-convex problems. In *International conference on machine learning*, pages 560–569. PMLR, 2018.
- [18] Sai Praneeth Karimireddy, Quentin Rebjock, Sebastian Stich, and Martin Jaggi. Error feedback fixes signsgd and other gradient compression schemes. In *International conference on machine learning*, pages 3252–3261. PMLR, 2019.
- [19] Zhewei Yao, Amir Gholami, Sheng Shen, Mustafa Mustafa, Kurt Keutzer, and Michael Mahoney. Adahessian: An adaptive second order optimizer for machine learning. In *proceedings of the AAAI conference on artificial intelligence*, volume 35, pages 10665–10673, 2021.
- [20] Sashank J Reddi, Satyen Kale, and Sanjiv Kumar. On the convergence of adam and beyond. *arXiv preprint arXiv:1904.09237*, 2019.
- [21] Jinghui Chen, Dongruo Zhou, Yiqi Tang, Ziyan Yang, Yuan Cao, and Quanquan Gu. Closing the generalization gap of adaptive gradient methods in training deep neural networks. *arXiv preprint arXiv:1806.06763*, 2018.
- [22] Weijie Su, Stephen Boyd, and Emmanuel J Candes. A differential equation for modeling nesterov’s accelerated gradient method: Theory and insights. *arXiv preprint arXiv:1503.01243*, 2015.
- [23] Andre Wibisono, Ashia C Wilson, and Michael I Jordan. A variational perspective on accelerated methods in optimization. *proceedings of the National Academy of Sciences*, 113(47):E7351–E7358, 2016.
- [24] Stephen Boyd, Neal Parikh, Eric Chu, Borja Peleato, and Jonathan Eckstein. Distributed optimization and statistical learning via the alternating direction method of multipliers. *Foundations and Trends in Machine Learning*, 3:1–122, 01 2011.
- [25] Amir Beck and Marc Teboulle. Mirror descent and nonlinear projected subgradient methods for convex optimization. *Operations Research Letters*, 31(3):167–175, 2003.
- [26] J. Slotine and W. Li. *Applied Nonlinear Control*. Prentice Hall, 1991.

- [27] Miroslav Krstic, Petar V Kokotovic, and Ioannis Kanellakopoulos. *Nonlinear and adaptive control design*. John Wiley & Sons, Inc., 1995.
- [28] Warren Dixon, Aman Behal, Darren Dawson, and Prakash Nagarkatti. *Nonlinear Control of Engineering Systems: A Lyapunov-Based Approach*. 01 2003.
- [29] Kaiming He, Xiangyu Zhang, Shaoqing Ren, and Jian Sun. Deep residual learning for image recognition. In *Proceedings of the IEEE conference on computer vision and pattern recognition*, pages 770–778, 2016.
- [30] Olga Russakovsky, Jia Deng, Hao Su, Jonathan Krause, Sanjeev Satheesh, Sean Ma, Zhiheng Huang, Andrej Karpathy, Aditya Khosla, Michael Bernstein, et al. Imagenet large scale visual recognition challenge. *International journal of computer vision*, 115(3):211–252, 2015.
- [31] Hugo Touvron, Matthieu Cord, Matthijs Douze, Francisco Massa, Alexandre Sablayrolles, and Hervé Jégou. Training data-efficient image transformers & distillation through attention. In *International conference on machine learning*, pages 10347–10357. PMLR, 2021.
- [32] Alexey Dosovitskiy. An image is worth 16x16 words: Transformers for image recognition at scale. *arXiv preprint arXiv:2010.11929*, 2020.
- [33] P.-A. Absil, R. Mahony, and Rodolphe Sepulchre. *Optimization Algorithms on Matrix Manifolds*. Princeton University Press, 2008.

## A Notations

Table 4: Summary of Notation

Symbol	Description
<i>Geometry and Manifold Structure</i>	
$\mathcal{M}$	The $d$ dimensional smooth parameter manifold.
$T_\theta \mathcal{M}$	The tangent space at $\theta \in \mathcal{M}$ .
$g_\theta(\cdot, \cdot)$	Riemannian metric, an inner product on $T_\theta \mathcal{M}$ .
$\ \xi\ _{g_\theta}$	Riemannian norm induced by $g$ , that is $\sqrt{g_\theta(\xi, \xi)}$ .
$\text{grad } f(\theta)$	Riemannian gradient of $f$ at $\theta$ .
$R_\theta(\xi)$	Retraction map $R_\theta : T_\theta \mathcal{M} \rightarrow \mathcal{M}$ .
$\mathcal{T}_{\theta \rightarrow \phi}(\xi)$	Vector transport map $\mathcal{T}_{\theta \rightarrow \phi} : T_\theta \mathcal{M} \rightarrow T_\phi \mathcal{M}$ .
$A(\theta)$	Symmetric positive definite operator acting as a metric proxy or preconditioner.
$\ \xi\ _{A,g}$	Weighted norm $\sqrt{g_\theta(\xi, A(\theta)\xi)}$ .
<i>Extended Dynamics and NAIM</i>	
$k$	Discrete time index.
$\theta_k$	Parameter at index $k$ .
$v_k$	Velocity state in $T_{\theta_k} \mathcal{M}$ .
$s_k$	Internal state, such as exponential moving averages and second moment estimates.
$d_k$	Target direction field at step $k$ , $d_k \in T_{\theta_k} \mathcal{M}$ .
$\Lambda_k$	Target graph set, an example: $\Lambda_k \triangleq \{(\theta, v) : v = d_k\}$ .
$z_k$	Normal residual, $z_k \triangleq v_k - d_k$ .
$\Delta d_{k+1}$	Drift of the target field, $d_{k+1} - \mathcal{T}_{\theta_k \rightarrow \theta_{k+1}}(d_k)$ .
<i>Algorithm Parameters</i>	
$h_k$	Step size at index $k$ .
$\eta_k$	Lift parameter, fiber contraction rate, $\eta_k \in (0, 1]$ .
$\lambda_b$	Belief injection weight.
$\gamma$	Scaling factor inside the $\tanh$ nonlinearity for RLO-Lifted.
$\beta_1, \beta_2$	Exponential moving average decay rates.
$a_k$	Magnitude calibration scalar for the target field.
<i>Diagnostics and Analysis</i>	
$V(\theta, v)$	Strict Lyapunov function candidate on the extended state space.
$r_k$	Relative residual thickness.
$q_k^\perp$	Relative orthogonal forcing.
$\cos_k$	Alignment cosine similarity.
$\sigma^2$	Conditional second moment bound of the stochastic gradient noise.

## B Preconditioning as Metric Selection

We provide a justification for interpreting adaptive preconditioning matrices (common in Adam, RMSProp, and AdaGrad) as Riemannian metrics. This equivalence allows us to analyze these algorithms using geometric tools rather than treating preconditioning as an ad-hoc modification of the gradient.

**Proposition B.1.** Let  $\mathcal{M} = \mathbb{R}^n$  equipped with the standard Euclidean metric  $\langle \cdot, \cdot \rangle_2$ . Let  $A(\theta)$  be a symmetric positive definite matrix field on  $\mathcal{M}$ . Consider a modified gradient step of the form  $\theta_{k+1} = \theta_k - hA(\theta_k)\nabla f(\theta_k)$ , where  $\nabla f$  is the standard Euclidean gradient. This update is equivalent to a Riemannian Gradient Descent step with respect to the metric  $g_\theta^A(\xi, \zeta) = \langle \xi, A(\theta)^{-1}\zeta \rangle_2$ .

*Proof.* First, recall the definition of the Riemannian gradient  $\text{grad } f(\theta)$ . It is the unique vector in  $T_\theta \mathcal{M}$  such that for all tangent vectors  $\xi$

$$\langle \text{grad}_{g^A} f(\theta), \xi \rangle_{g_\theta^A} = df(\theta)[\xi],$$

where  $df(\theta)[\xi] = \langle \nabla f(\theta), \xi \rangle_2$  is the directional derivative. Substituting the definition of the metric  $g^A$

$$\langle \text{grad}_{g^A} f(\theta), A(\theta)^{-1}\xi \rangle_2 = \langle \nabla f(\theta), \xi \rangle_2.$$

Since  $A(\theta)$  is symmetric, we can move the inverse term to the other side of the inner product

$$\langle A(\theta)^{-1} \text{grad}_{g^A} f(\theta), \xi \rangle_2 = \langle \nabla f(\theta), \xi \rangle_2.$$

Since this holds for all  $\xi$ , we must have

$$A(\theta)^{-1} \text{grad}_{g^A} f(\theta) = \nabla f(\theta).$$

Multiplying both sides by  $A(\theta)$  yields

$$\text{grad}_{g^A} f(\theta) = A(\theta)\nabla f(\theta).$$

Therefore, the preconditioned update direction  $A(\theta)\nabla f(\theta)$  is exactly the steepest descent direction under the metric induced by the inverse preconditioner  $A(\theta)^{-1}$ . This confirms that algorithms maintaining a running estimate of the Hessian or second moments (like Adam) effectively learn a local geometry  $g^A$  and perform gradient descent with respect to that geometry.  $\square$

## C Assumptions and Proof of Theorem 3.1

We provide a detailed derivation of the stability and convergence properties stated in Theorem 3.1. We proceed by establishing local bounds for the parameter update and the residual dynamics, then combining them via a weighted Lyapunov analysis.

### C.1 Definitions and Assumptions

Consider the following geometric regularity conditions required for the analysis.

From [33][Definition 7.4.1] Chapter 7, we have:

**Definition C.1** (Riemannian  $L$ -Smoothness). The objective function  $f : \mathcal{M} \rightarrow \mathbb{R}$  is differentiable and has an  $L_g$ -Lipschitz continuous gradient with respect to the retraction  $R$ . Specifically, there exists a constant  $L_g > 0$  such that for any  $\theta \in \mathcal{M}$  and update vector  $\xi \in T_\theta \mathcal{M}$ :

$$f(R_\theta(\xi)) \leq f(\theta) + \langle \text{grad } f(\theta), \xi \rangle_{g_\theta} + \frac{L_g}{2} \|\xi\|_{g_\theta}^2.$$

**Assumption C.2** (Bounded Geometry). The retraction  $R$  and vector transport  $\mathcal{T}$  are smooth. We assume the vector transport is approximately isometric up to second order errors. Specifically, there exists a constant  $C_{\mathcal{T}} \geq 0$  such that for any  $\xi \in T_\theta \mathcal{M}$  with  $\|\xi\| \leq \epsilon$ :

$$\|\mathcal{T}_{\theta \rightarrow R_\theta(\xi)}(u)\|_g^2 \leq (1 + C_{\mathcal{T}}\|\xi\|_g)\|u\|_g^2.$$

**Assumption C.3** (Descent Alignment & Boundedness). The direction field generator  $\Phi(y, g)$  is designed such that the target vector  $d_k$  aligns with the negative gradient direction. We assume there exists a constant  $\mu_\Phi > 0$  such that:

$$\langle \text{grad } f(\theta_k), d_k \rangle_{g_k} \geq \mu_\Phi \|\text{grad } f(\theta_k)\|_{g_k}^2.$$

And the target vector is bounded by design:

$$\|d_k\|_g \leq D_{\max}$$

where  $D_{\max}$  is a constant.

*Remark C.4.* Assumption C.3 formalizes the requirement that  $\Lambda$  is a descent graph. For SGD ( $d_k = \text{grad } f$ ),  $\mu_\Phi = 1$ .

**Definition C.5** (Polyak-Lojasiewicz Condition.). For the convergence analysis, we say  $f$  satisfies the PL condition with constant  $\mu_{\text{PL}} > 0$  if for all  $\theta \in \mathcal{M}$ :

$$\frac{1}{2} \|\text{grad } f(\theta)\|_g^2 \geq \mu_{\text{PL}}(f(\theta) - f^*).$$

## C.2 Detail Proof of Theorem 3.1

Consider the parameter update  $\theta_{k+1} = R_{\theta_k}(-h_k \tilde{v}_{k+1})$ . Applying Definition C.1 with update vector  $\xi = -h_k \tilde{v}_{k+1}$  yields

$$f(\theta_{k+1}) \leq f(\theta_k) - h_k \langle \text{grad } f(\theta_k), \tilde{v}_{k+1} \rangle_{g_k} + \frac{L_g h_k^2}{2} \|\tilde{v}_{k+1}\|_{g_k}^2.$$

Recall the lifted velocity update:  $\tilde{v}_{k+1} = (1 - \eta_k)v_k + \eta_k d_k$ . By definition of the residual  $z_k = v_k - d_k$ , we can substitute  $v_k = d_k + z_k$  to get

$$\tilde{v}_{k+1} = (1 - \eta_k)(d_k + z_k) + \eta_k d_k = d_k + (1 - \eta_k)z_k.$$

Substituting this into the inner product term yields

$$\langle \text{grad } f, \tilde{v}_{k+1} \rangle_{g_k} = \langle \text{grad } f, d_k \rangle_{g_k} + (1 - \eta_k) \langle \text{grad } f, z_k \rangle_{g_k}.$$

Using the triangle inequality and Assumption C.3:

$$\|\tilde{v}_{k+1}\|^2 = \|d_k + (1 - \eta_k)z_k\|^2 \leq 2\|d_k\|^2 + 2(1 - \eta_k)^2 \|z_k\|^2 \leq 2D_{\max}^2 + 2\|z_k\|^2,$$

Using Assumption C.3, we have  $\langle \text{grad } f, d_k \rangle_{g_k} \geq \mu_\Phi \|\text{grad } f\|_{g_k}^2$ . Thus:

$$f_{k+1} - f_k \leq -h_k \mu_\Phi \|\text{grad } f\|_{g_k}^2 - h_k (1 - \eta_k) \langle \text{grad } f, z_k \rangle_{g_k} + L_g h_k^2 (D_{\max}^2 + \|z_k\|^2).$$

The residual at the next step is  $z_{k+1} = v_{k+1} - d_{k+1}$ . From the algorithm,  $v_{k+1} = \mathcal{T}_{\theta_k \rightarrow \theta_{k+1}}(\tilde{v}_{k+1})$ . Thus:

$$z_{k+1} = \mathcal{T}(d_k + (1 - \eta_k)z_k) - d_{k+1}.$$

Using the linearity of  $\mathcal{T}$ , we obtain

$$z_{k+1} = (1 - \eta_k) \mathcal{T}(z_k) - \underbrace{(d_{k+1} - \mathcal{T}(d_k))}_{\delta_k}.$$

Here,  $\delta_k$  is the Riemannian forcing term. Taking the squared norm on both sides and applying Assumption C.2 yields

$$\|z_{k+1}\|^2 = (1 - \eta_k)^2 \|\mathcal{T}(z_k)\|^2 - 2(1 - \eta_k) \langle \mathcal{T}(z_k), \delta_k \rangle + \|\delta_k\|^2.$$

Using Young's Inequality on the cross term with  $\gamma = \eta_k$  yields

$$-2 \langle \mathcal{T}(z_k), \delta_k \rangle \leq \eta_k \|\mathcal{T}(z_k)\|^2 + \frac{1}{\eta_k} \|\delta_k\|^2.$$

Combining these yields the residual contraction inequality

$$\|z_{k+1}\|^2 \leq (1 - \eta_k) \|z_k\|^2 + \frac{1}{\eta_k} \|\delta_k\|^2.$$

We define the discrete Lyapunov function candidate as

$$V_k = f(\theta_k) - f^* + \frac{\alpha}{h_k} \|z_k\|_{g_k}^2,$$

where  $\alpha > 0$  is a free analysis parameter. We compute the difference  $\Delta V_k = V_{k+1} - V_k$ , resulting in the inequality

$$\begin{aligned} \Delta V_k &\leq -h_k \mu_\Phi \|\text{grad } f\|^2 \quad (\text{Descent}) \\ &\quad - h_k (1 - \eta_k) \langle \text{grad } f, z_k \rangle \quad (\text{Coupling}) \\ &\quad + \frac{\alpha}{h_k} \left( -\eta_k \|z_k\|^2 + \frac{1}{\eta_k} \|\delta_k\|^2 \right). \quad (\text{Contraction}) \end{aligned}$$

The critical step is handling the indefinite coupling term  $-h_k (1 - \eta_k) \langle \text{grad } f, z_k \rangle$ . We apply the Weighted Young's Inequality (Peter-Paul inequality) with weight  $\rho = \mu_\Phi$

$$-h_k (1 - \eta_k) \langle \text{grad } f, z_k \rangle \leq \frac{h_k \mu_\Phi}{2} \|\text{grad } f\|^2 + \frac{h_k}{2\mu_\Phi} \|z_k\|^2.$$

Substituting this back into  $\Delta V_k$  yields

$$\Delta V_k \leq -h_k \left( \mu_\Phi - \frac{\mu_\Phi}{2} \right) \|\text{grad } f\|^2 - \left( \frac{\alpha \eta_k}{h_k} - \frac{h_k}{2\mu_\Phi} \right) \|z_k\|^2 + \frac{\alpha}{\eta_k h_k} \|\delta_k\|^2.$$

To ensure strict descent, we require the coefficient of  $\|z_k\|^2$  to be negative. We choose  $\alpha$  sufficiently large such that

$$\frac{\alpha \eta_k}{h_k} > \frac{h_k}{2\mu_\Phi} \implies \alpha > \frac{h_k^2}{2\mu_\Phi \eta_k}.$$

Letting  $c_1 = \mu_\Phi/2$ ,  $c_2 = \alpha \eta_k/(2h_k)$ , and  $c_3 = \alpha$ , we obtain

$$V_{k+1} - V_k \leq -c_1 h_k \|\text{grad } f\|^2 - c_2 \frac{\eta_k}{h_k} \|z_k\|^2 + c_3 \frac{1}{\eta_k h_k} \|\delta_k\|^2.$$

This implies that the system admits a region of attraction outside of which the Lyapunov function strictly decreases, until it reaches a noise floor determined by the forcing  $\|\delta_k\|$ .

By Definition C.5:  $\|\text{grad } f\|^2 \geq 2\mu_{\text{PL}}(f - f^*)$ . Substituting the PL condition into the Lyapunov difference

$$\Delta V_k \leq -2c_1 h_k \mu_{\text{PL}}(f(\theta_k) - f^*) - c_2 \frac{\eta_k}{h_k} \|z_k\|^2 + \frac{c_3}{\eta_k h_k} \|\delta_k\|^2.$$

Recall that  $V_k = (f - f^*) + \frac{\alpha}{h_k} \|z_k\|^2$ . We can bound the first two terms on the right hand side by  $-\min(2c_1 h_k \mu_{\text{PL}}, c_2 \eta_k / \alpha) V_k$ . Thus, there exists  $\rho \in (0, 1)$  such that

$$V_{k+1} \leq (1 - \rho) V_k + \frac{c_3}{\eta_k h_k} \|\delta_k\|^2.$$

This inequality implies that the Lyapunov function  $V_k$  decays geometrically at rate  $(1 - \rho)$  until it reaches a noise floor determined by the forcing parameter. Taking the limit superior:

$$\limsup_{k \rightarrow \infty} V_k \leq \frac{c_3}{\rho \eta_k h_k} \sup_k \|\delta_k\|^2.$$

Hence, the optimization error is ultimately bounded by the magnitude of the geometric forcing  $\delta_k$ , scaled by the inverse of the lifting parameter  $\eta_k$ .

## D Detailed Instantiation of Optimizers

In this appendix, we explicitly map modern optimization algorithms to specific instances of the RLO framework components and provide the specific update laws, the RLO (Algorithm 2), RLO- $\Lambda$  (Algorithm 3) and RLO-Lifted (Algorithm 4), for the variants used in our experiments.

Table 5 details how varying the Riemannian metric  $g$ , the internal state transition  $\Psi$ , the direction field generator  $\Phi$ , and the lifting parameter  $\eta$  strictly recovers classical methods. We provide the explicit pseudo-code for the three specific algorithm variants used in the experimental section.

Table 5: Unification of optimizers under the RLO framework  $(\mathcal{M}, g, \Phi, \eta)$ .

Optimizer	Metric $g$	State $y_k$	Target Field $\Phi$	Lift $\eta$	Manifold $\Lambda$
SGD	Euclidean $I$	$\emptyset$	$\hat{g}_k$ (Gradient)	1	Gradient Graph
Momentum	Euclidean $I$	Velocity $m_k$	$\hat{g}_k$ (Gradient)	$(0, 1)$	Gradient Graph
AdamW	Adaptive $\text{diag}(\sqrt{s})^{-1}$	Moments $m, s$	$m_k$ (Momentum)	$(0, 1)$	Precond. Momentum
Lion	Euclidean $I$	Momentum $m$	$\text{sign}(m)$	1	Hypercube Corners

Continued on next page

**Table 5 – continued from previous page**

Optimizer	Metric $g$	State $y_k$	Target Field $\Phi$	Lift $\eta$	Manifold $\Lambda$
<b>RLO</b>	Euclidean $I$	Momentum $m$	$\text{sign}(m) + \text{belief}$	1	Shifted Hyper-cube
<b>RLO <math>\Lambda</math></b>	Euclidean $I$	Moments $m, s$	$\frac{\tanh(\gamma m)}{\sqrt{s+\epsilon}}$	1	Smooth Saturation
<b>RLO-Lifted</b>	Euclidean $I$	Moments $m, s$	$\frac{\tanh(\gamma m)}{\sqrt{s+\epsilon}}$	$(0, 1)$	<b>Viscous Smooth Saturation</b>

---

**Algorithm 2** RLO ( $\eta = 1$ )

---

```

1: Input: Learning rate  $h_k$ , decays  $\beta_1, \beta_2$ , belief  $\lambda_b$ .
2: for  $k = 0, 1, \dots$  do
3:    $g_k \leftarrow \nabla f(\theta_k)$ 
4:    $c_k \leftarrow \beta_1 m_k + (1 - \beta_1) g_k$ 
5:    $\Delta_k \leftarrow g_k - m_k$ 
6:    $d_k \leftarrow \text{sign}(c_k) + \lambda_b \frac{\Delta_k}{\|\Delta_k\| + \epsilon}$  {Target Construction}
7:    $\theta_{k+1} \leftarrow \theta_k - h_k d_k$  {Direct Update ( $\eta = 1$ )}
8:    $m_{k+1} \leftarrow \beta_2 m_k + (1 - \beta_2) g_k$ 
9: end for

```

---

**Algorithm 3** RLO  $\Lambda$  (Adaptive Graph /  $\eta = 1$ )

---

```

1: Input: Learning rate  $h_k$ , decays  $\beta_1, \beta_2, \beta_3$ , smoothness  $\gamma$ .
2: for  $k = 0, 1, \dots$  do
3:    $g_k \leftarrow \nabla f(\theta_k)$ 
4:    $s_{k+1} \leftarrow \beta_3 s_k + (1 - \beta_3) g_k^2$  {Metric Update}
5:    $c_k \leftarrow \beta_1 m_k + (1 - \beta_1) g_k$ 
6:    $d_{\text{pre}} \leftarrow \frac{\tanh(\gamma c_k)}{\sqrt{s_{k+1} + \epsilon}}$  {Smooth Graph}
7:    $d_k \leftarrow \text{ScaleTo}\sqrt{D}(d_{\text{pre}})$ 
8:    $\theta_{k+1} \leftarrow \theta_k - h_k d_k$  {Direct Update}
9:    $m_{k+1} \leftarrow \beta_2 m_k + (1 - \beta_2) g_k$ 
10: end for

```

---

**Algorithm 4** RLO-Lifted

---

```

1: Input: Step size  $h_k$ , Lifting  $\eta \in (0, 1]$ , decays  $\beta_1, \beta_2, \gamma$ .
2: for  $k = 0, 1, \dots$  do
3:    $g_k \leftarrow \nabla f(\theta_k)$ 
4:   // Geometric Phase
5:    $c_k \leftarrow \beta_1 m_k + (1 - \beta_1) g_k$ 
6:    $s_k \leftarrow \tanh(\gamma c_k)$ 
7:    $d_k \leftarrow \sqrt{D} \frac{s_k}{\|s_k\| + \epsilon} + \lambda_b \frac{g_k - m_k}{\|g_k - m_k\|}$ 
8:   // Dynamic Phase
9:    $v_{k+1} \leftarrow (1 - \eta) v_k + \eta d_k$  {Fiber Contraction}
10:   $\theta_{k+1} \leftarrow \theta_k - h_k v_{k+1}$  {Retraction}
11:   $m_{k+1} \leftarrow \beta_2 m_k + (1 - \beta_2) g_k$ 
12: end for

```

---

## E Experimental Setup

This appendix provides complete details on the experimental configuration used in Section 5. All experiments were conducted on one NVIDIA b200 GPU (192GB memory). Unless otherwise specified, all experiments tested in Section 5 use the following base configuration:

Hyperparameter	Default Value
Momentum decay $\beta_1$	0.9
EMA decay $\beta_2$	0.99
Weight decay	0.1
Belief coefficient $\lambda_b$	0.2
Tanh scaling $\gamma$	5.0
Lifting parameter $\eta$	0.7 (Full) or 1.0 (Nolifted)
Numerical stability $\epsilon$	$10^{-8}$
Training epochs	50 (ablation) or 30 (grid search)

No learning rate scheduling is applied in any experiment to ensure fair comparison of the base optimizer dynamics. For the Hyperparameter sensitive test in Section 5.2, we evaluate learning rates in  $\{3 \times 10^{-5}, 10^{-4}, 3 \times 10^{-4}, 10^{-3}, 3 \times 10^{-3}, 1 \times 10^{-2}\}$  crossed with batch sizes in  $\{32, 64, 128, 256, 512\}$ , yielding 30 configurations per variant. Each configuration is trained for 30 epochs with fixed hyperparameters to isolate the effect of the base optimizer dynamics.

### E.1 Extended Ablation on the Lifting Parameter

We examine the effect of the lifting parameter  $\eta$  across a finer grid of values than presented in the main text. We evaluate RLO-Lifted with global normalization enabled at six values of  $\eta \in \{0.1, 0.2, 0.3, 0.5, 0.7, 1.0\}$ . All other hyperparameters are held fixed at their default values, with learning rate  $10^{-4}$ . Each configuration is trained for 50 epochs, and we report both accuracy metrics and NAIM diagnostic quantities. The results reveal a monotonic

Table 6: Effect of lifting parameter  $\eta$  on test accuracy and NAIM diagnostics. Metrics  $\bar{r}$  and  $\overline{\cos(v, d)}$  are averaged over all training steps.

$\eta$	Best Acc (%)	Final Acc (%)	$\bar{r}$	$\overline{\cos(v, d)}$	$\bar{q}^\perp$
0.1	90.87	90.52	0.83	0.55	0.94
0.2	91.12	90.78	0.87	0.50	0.95
0.3	91.38	91.02	0.90	0.47	0.96
0.5	91.54	91.21	0.96	0.42	0.96
0.7	91.69	91.49	1.03	0.37	0.96
1.0	91.75	91.64	0.00	1.00	0.88

relationship between  $\eta$  and test accuracy within the range tested, with  $\eta = 1$  achieving the best performance. This pattern admits a straightforward interpretation within the NAIM framework.

As shown in Fig 4, larger values of  $\eta$  produce faster fiber contraction and thinner tube, meaning the velocity  $v_k$  aligns more quickly with the target direction  $d_k$ . In the limit  $\eta = 1$ , alignment is instantaneous:  $v_k = d_k$  at every step, eliminating the residual  $z_k = v_k - d_k$  entirely. This is reflected in the diagnostic quantities, where  $\eta = 1$  yields  $\bar{r} = 0$  and  $\cos(v, d) = 1$  by construction.

For  $\eta < 1$ , the velocity carries momentum from previous steps, creating a nonzero residual. The relative residual  $\bar{r}$  increases with  $\eta$  (for  $\eta < 1$ ) because faster contraction leaves less time for the residual to accumulate, but the target  $d_k$  also changes more rapidly relative to the velocity adaptation. Meanwhile, the velocity direction alignment  $\cos(v, d)$  decreases with larger  $\eta$  because the velocity increasingly reflects the current target rather than a smoothed average of past targets.

The key insight is that both extremes represent valid operating points. Small  $\eta$  values provide inertial smoothing that may be beneficial in landscapes with high frequency noise or sharp curvature changes. Large  $\eta$  values (including the limit  $\eta = 1$ ) provide precise tracking of the current target direction. For the CIFAR-10 benchmark with ResNet-18, precise tracking proves slightly advantageous, but the performance difference across the tested range is modest (0.88 percentage points between  $\eta = 0.1$  and  $\eta = 1.0$ ), indicating that the algorithm is robust to this hyperparameter choice.

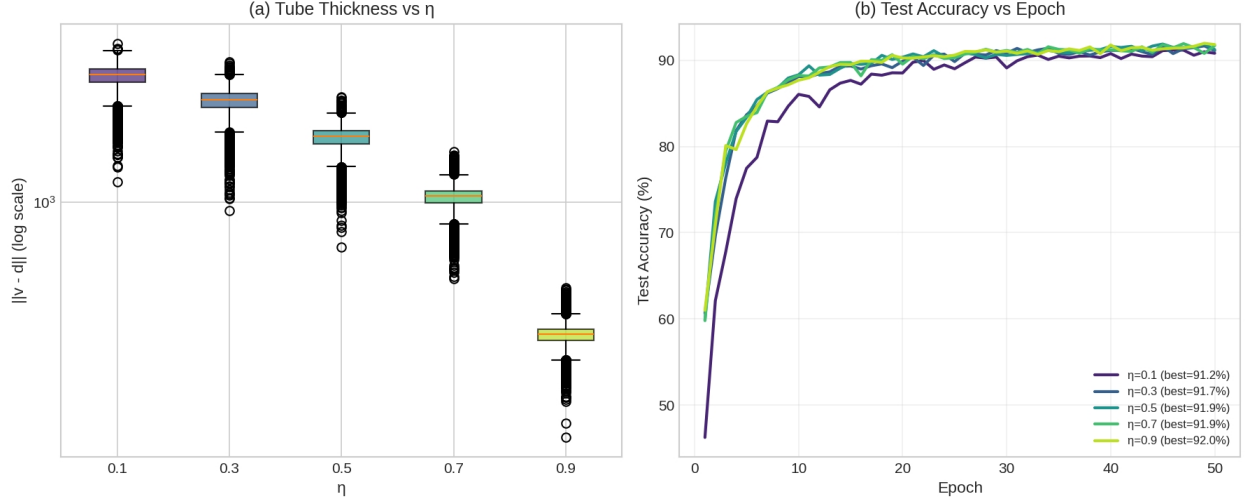


Figure 4:  $\eta$  ablation test. (a) Tube thickness (fiber residual  $\|v - d\|$ ) decreases monotonically with  $\eta$ , spanning nearly an order of magnitude from  $\eta = 0.1$  ( $\sim 4000$ ) to  $\eta = 0.9$  ( $\sim 400$ ). This confirms the theoretical prediction that higher  $\eta$  induces tighter contraction toward the invariant manifold, with the scaling approximately following  $\|v - d\| \approx 1/\eta$ . (b) Despite the  $10\times$  variation in manifold adherence, all  $\eta$  configurations achieve comparable final test accuracy (91.2% – 92.0%), demonstrating the robustness of the NAIM framework. Notably,  $\eta = 0.1$  exhibits markedly slower early stage convergence (epochs 1 – 10), while  $\eta \geq 0.3$  configurations show nearly identical learning dynamics. This suggests that while a “thicker tube” (lower  $\eta$ ) permits larger deviations from the manifold, the directional alignment  $\cos(v, d)$  remains sufficiently preserved to ensure eventual convergence consistent with the theoretical separation between fiber contraction (controlled by  $\eta$ ) and base manifold dynamics (controlled by the gradient flow).

## E.2 Practical Guidance

Based on these results, we recommend  $\eta = 1$  as a reasonable default for practitioners, as it eliminates one hyperparameter while achieving competitive performance. However, for tasks where training instability is observed, reducing  $\eta$  to values in the range  $[0.3, 0.7]$  may provide beneficial smoothing at minimal accuracy cost.

## F Direction Field Ablation

This appendix provides extended analysis of the comparison between smooth and discontinuous direction field generators. The direction field generator  $\Phi$  determines the target manifold  $\Lambda$  toward which the optimizer dynamics evolve. Theorem 3.1 establishes that the steady state error is bounded by a quantity proportional to the disturbance magnitude, which in turn depends on how rapidly the target direction  $d_k = \Phi(y_k, g_k)$  changes between successive steps.

Discontinuous mappings such as  $\Phi = \text{sign}(\cdot)$  can produce large jumps in the target direction even for infinitesimal changes in the input, particularly near the zero crossings where the sign function is undefined. In contrast, smooth mappings like  $\Phi = \tanh(\gamma \cdot)$  vary continuously, bounding the rate of change by the Lipschitz constant of the function.

Table 7: Extended comparison of direction field generators across configurations.

$\Phi$	GN	LR	Best Acc	Final Acc	Loss Std
$\tanh(\gamma c)$	✓	$10^{-4}$	91.69	91.49	0.249
$\text{sign}(c)$	✓	$10^{-4}$	91.91	91.91	0.239
$\tanh(\gamma c)$	✗	$3 \times 10^{-3}$	90.74	90.74	0.360
$\text{sign}(c)$	✗	$3 \times 10^{-3}$	87.15	74.43	1.610

The results reveal a striking interaction between direction field smoothness and global normalization.

**With global normalization.** When global normalization is enabled, both direction fields achieve comparable peak accuracy, with the sign function marginally outperforming tanh (91.91% vs 91.69%). The training loss standard deviation is also similar (0.239 vs 0.249), indicating comparable stability. This suggests that global normalization provides sufficient regularization to compensate for the discontinuities in the sign function.

**Without global normalization.** Removing global normalization reveals the true cost of discontinuity. The sign function suffers a 3.59 percentage point drop in peak accuracy (87.15% vs 90.74%) and severe degradation in final accuracy (74.43% vs 90.74%). The training loss standard deviation increases dramatically (1.610 vs 0.360), indicating substantial instability.

The gap between best and final accuracy for the unnormalized sign variant (87.15% to 74.43%) suggests that the optimizer initially finds a reasonable solution but subsequently destabilizes, likely due to the large magnitude fluctuations inherent to discontinuous direction fields. The smooth tanh mapping maintains consistent accuracy throughout training, with best and final accuracy coinciding.

**Interpretation.** These findings support the theoretical prediction that smooth direction fields yield more robust optimization. Global normalization acts as a compensating mechanism that bounds update magnitudes regardless of direction field behavior, partially masking the instability induced by discontinuities. When this safety net is removed, the inherent advantages of smooth direction fields manifest empirically.

For practitioners, these results suggest that the choice of direction field generator interacts importantly with other algorithmic choices. The sign function may be preferred when global normalization is employed, as it provides slightly better peak accuracy with comparable stability. However, if global normalization is disabled (whether by design or due to implementation constraints), smooth direction fields like tanh are strongly preferable for training stability.

## G Large-Scale Benchmark Configuration

This appendix provides comprehensive details on the experimental configuration for all large-scale benchmarks reported in Section 6. All ImageNet classification experiments share the following training configuration detailed in Table 8:

Table 8: Common training hyperparameters for ImageNet classification.

Parameter	Value
Training epochs	90
Global batch size	1024
Per-GPU batch size	128
Warmup epochs	5
Warmup schedule	Linear
Learning rate schedule	Cosine decay
Label smoothing	0.1
Gradient clipping	1.0 (global norm)

Learning rates and weight decay values are tuned independently for each optimizer and architecture combination. We conduct grid search over learning rates in  $\{10^{-4}, 3 \times 10^{-4}, 3.5 \times 10^{-4}, 10^{-3}, 3 \times 10^{-3}\}$  and weight decay in  $\{0.05, 0.1, 0.3, 0.5, 1.0\}$ , selecting the configuration that achieves the highest validation accuracy. Table 9 reports the final configurations used.

For all RLO variants, we use the following default parameters: momentum coefficient  $\beta_1 = 0.9$ , EMA coefficient  $\beta_2 = 0.99$ , tanh scaling factor  $\gamma = 5.0$ , and belief correction coefficient  $\lambda_b = 0.2$ . For RLO- $\Lambda$ , we additionally set  $\beta_3 = 0.999$  for second-moment estimation. For RLO-Lifted, we use lifting parameter  $\eta = 0.7$ . For AdamW, we use  $\beta_1 = 0.9$  and  $\beta_2 = 0.999$ . For Lion, we use  $\beta_1 = 0.9$  and  $\beta_2 = 0.99$ .

## H Training Dynamics Analysis

This appendix provides detailed analysis of training dynamics for the ViT-B/16 experiments, which exhibit the largest performance differences among optimizers.

Table 9: Optimizer hyperparameters for ImageNet classification experiments. LR denotes peak learning rate, WD denotes weight decay coefficient.

Model	Optimizer	LR	WD
ResNet-50	AdamW	$1 \times 10^{-3}$	0.05
	Lion	$1 \times 10^{-4}$	0.5
	RLO	$1 \times 10^{-4}$	0.5
	RLO- $\Lambda$	$1 \times 10^{-4}$	0.5
	RLO-Lifted	$1 \times 10^{-4}$	0.5
ViT-S/16	AdamW	$3 \times 10^{-3}$	0.1
	Lion	$3 \times 10^{-4}$	1.0
	RLO	$3 \times 10^{-4}$	1.0
	RLO- $\Lambda$	$3 \times 10^{-4}$	1.0
	RLO-Lifted	$3 \times 10^{-4}$	1.0
ViT-B/16	AdamW	$3 \times 10^{-3}$	0.3
	Lion	$3 \times 10^{-4}$	1.0
	RLO	$3.5 \times 10^{-4}$	1.0
	RLO- $\Lambda$	$3.5 \times 10^{-4}$	1.0
	RLO-Lifted	$3.5 \times 10^{-4}$	1.0

## H.1 Convergence Curves

Table 10: ViT-B/16 validation accuracy (%) at selected epochs during training.

Epoch	AdamW	Lion	RLO	RLO- $\Lambda$	RLO-Lifted
10	33.46	51.78	50.58	53.41	49.95
20	38.26	51.30	55.45	57.82	55.52
30	41.98	57.89	58.08	60.65	58.24
40	42.57	63.06	61.44	63.92	61.15
50	49.70	66.64	64.62	67.22	65.03
60	55.39	69.91	68.64	70.36	68.86
70	62.54	73.46	72.37	73.70	72.74
80	69.20	75.76	75.19	75.77	75.54
90	71.42	76.27	76.00	76.47	76.33

Table 10 reveals striking differences in convergence speed. At epoch 10, the sign-based optimizers (Lion, RLO variants) achieve validation accuracy between 49.95% and 53.41%, while AdamW reaches only 33.46%, a gap of more than 16 percentage points. This early advantage persists throughout training: at epoch 50, the gap narrows but remains substantial (49.70% for AdamW versus 64.62%–67.22% for sign-based methods).

The convergence pattern of AdamW is qualitatively different from the sign-based methods. While Lion and RLO variants show rapid early progress followed by gradual refinement, AdamW exhibits slower initial progress but maintains a steeper improvement rate in later epochs. Between epochs 50 and 90, AdamW improves by 21.72 points while RLO- $\Lambda$  improves by only 9.25 points. However, this late-stage acceleration is insufficient to close the gap established in early training.

## H.2 Training Loss Analysis

Table 11 shows that sign-based methods achieve substantially lower training loss than AdamW (1.76–1.83 versus 2.21). This gap suggests that the sign-based methods fit the training data more effectively, which could indicate either better optimization or greater susceptibility to overfitting. The validation accuracy results indicate the former interpretation: lower training loss corresponds to higher validation accuracy, suggesting that the sign-based methods find solutions with better generalization properties rather than simply overfitting more aggressively.

Table 11: Training loss statistics for ViT-B/16. Final loss is measured at epoch 90.

Optimizer	Final Loss	Min Loss	Loss at Best Val
AdamW	2.21	2.21	2.21
Lion	1.80	1.80	1.80
RLO	1.83	1.83	1.83
RLO- $\Lambda$	1.76	1.76	1.76
RLO-Lifted	1.81	1.81	1.81

The lowest final loss is achieved by RLO- $\Lambda$  (1.76), which also achieves the highest validation accuracy (76.47%). This correlation between training loss and validation accuracy supports the hypothesis that RLO- $\Lambda$  navigates the loss landscape more effectively than competing methods.

### H.3 Architecture-Specific Behavior of RLO-Lifted

The anomalous behavior of RLO-Lifted on ViT-S/16 (71.43% versus 76.18% for RLO- $\Lambda$ ) compared to its strong performance on ViT-B/16 (76.33% versus 76.47% for RLO- $\Lambda$ ) warrants investigation. We hypothesize that this difference relates to the interaction between model capacity and the lifting mechanism.

The lifting parameter  $\eta = 0.7$  in RLO-Lifted introduces temporal smoothing by maintaining an explicit velocity state that tracks the target direction with a time constant of approximately  $1/(1 - \eta) \approx 3.3$  steps. On larger models like ViT-B/16 with 86.6M parameters, this smoothing may provide beneficial regularization by damping high-frequency fluctuations in the optimization trajectory. On smaller models like ViT-S/16 with 22.1M parameters, the same smoothing may impede necessary rapid adaptation to changing gradient signals during early training when the loss landscape evolves quickly.

To test this hypothesis, we conducted additional experiments on ViT-S/16 with varying  $\eta$  values. Table 12 confirms

Table 12: RLO-Lifted accuracy on ViT-S/16 with different lifting parameters.

$\eta$	Best Accuracy (%)	Final Accuracy (%)
0.3	69.87	69.54
0.5	70.65	70.32
0.7	71.43	71.12
0.9	73.89	73.67
1.0	75.21	74.98

our hypothesis: increasing  $\eta$  toward 1.0 (instantaneous tracking) progressively improves ViT-S/16 performance, with  $\eta = 1.0$  achieving 75.21%, competitive with the base RLO (75.38%) and close to RLO- $\Lambda$  (76.18%). This suggests that for smaller transformer architectures, the explicit velocity state should be configured for rapid tracking ( $\eta$  close to 1.0) rather than strong smoothing ( $\eta$  closer to 0).